Science Bulletin 69 (2024) 2187–2193

Contents lists available at ScienceDirect

Science Bulletin

journal homepage: www.elsevier.com/locate/scib

Article

Observation of 3D acoustic quantum Hall states

Xuewei Zhang [a,b,1], Qiang Wei [a,b,1], Mian Peng [a,b], Weiyin Deng [c], Jiuyang Lu [c], Xueqin Huang [c], Suotang Jia [a,b], Mou Yan [d,e,f,*], Zhengyou Liu [g,h,*], Gang Chen [a,b,d,e,f,*]

[a] State Key Laboratory of Quantum Optics and Quantum Optics Devices, Institute of Laser Spectroscopy, Shanxi University, Taiyuan 030006, China
[b] Collaborative Innovation Center of Extreme Optics, Shanxi University, Taiyuan 030006, China
[c] School of Physics and Optoelectronics, South China University of Technology, Guangzhou 510640, China
[d] Key Laboratory of Materials Physics, Ministry of Education, School of Physics, Zhengzhou University, Zhengzhou 450001, China
[e] Laboratory of Zhongyuan Light, School of Physics, Zhengzhou University, Zhengzhou 450001, China
[f] Institute of Quantum Materials and Physics, Henan Academy of Sciences, Zhengzhou 450046, China
[g] Key Laboratory of Artificial Micro- and Nanostructures of Ministry of Education and School of Physics and Technology, Wuhan University, Wuhan 430072, China
[h] Institute for Advanced Studies, Wuhan University, Wuhan 430072, China

ARTICLE INFO

Article history:
Received 28 December 2023
Received in revised form 4 February 2024
Accepted 23 April 2024
Available online 26 April 2024

Keywords:
Quantum Hall effects
Acoustic crystals
Pseudo-magnetic field
Landau levels
Edge states

ABSTRACT

Quantum Hall effect, the quantized transport phenomenon of electrons under strong magnetic fields, remains one of the hottest research topics in condensed matter physics since its discovery in 2D electronic systems. Recently, as a great advance in the research of quantum Hall effects, the quantum Hall effect in 3D systems, despite its big challenge, has been achieved in the bulk $ZrTe_5$ and Cd_3As_2 materials. Interestingly, Cd_3As_2 is a Weyl semimetal, and quantum Hall effect is hosted by the Fermi arc states on opposite surfaces via the Weyl nodes of the bulk, and induced by the unique edge states on the boundaries of the opposite surfaces. However, such intriguing edge state distribution has not yet been experimentally observed. Here, we aim to reveal experimentally the unusual edge states of Fermi arcs in acoustic Weyl system with the aid of pseudo-magnetic field. Benefiting from the macroscopic nature of acoustic crystals, the pseudo-magnetic field is introduced by elaborately designed the gradient on-site energy, and the edge states of Fermi arcs on the boundaries of the opposite surfaces are unambiguously demonstrated in experiments. Our system serves as an ideal and highly tunable platform to explore the Hall physics in 3D system, and has the potential in the application of new acoustic devices.

1. Introduction

Quantum Hall effect (QHE), observed in the two-dimensional (2D) electronic gas, is one of the greatest discoveries in the field of condensed matter physics, and opened the door to topological physics [1–8]. The quantized electronic transport in QHE roots in the chiral edge states, which can survive the disorders and impurities and thus become the core of the research for low-loss devices [9–11]. With the great success in the understanding of the 2D QHE, a fundamental and important question is raised: can this effect be found in 3D materials? For the 3D electron gases, QHE is commonly considered to be forbidden, since the Landau levels extend to bands due to the additional degree of freedom in the direction of the magnetic field, preventing the opening of the bulk gap. Despite tremendous effort by predecessors [12–17], the existence of 3D QHE remains elusive.

Recently, some pioneering experiments that capture the signature of 3D QHE have been reported [18–22]. One of them is based on the Weyl semimetals [22,23]. The Weyl semimetals host bulk bands touching at the discrete points, which have nonzero Berry curvatures and are dubbed Weyl points [24–26]. The most salient feature of Weyl semimetals is the existence of the Fermi arcs on two opposite surfaces, which can form a closed Fermi loop assisted by a pair of Weyl points of opposite charges. Under the external magnetic field, the Fermi loop becomes the Landau plateaus which deform near the boundaries of the surfaces, resulting in the 1D edge states. In contrast to 2D case, it is fascinating that the edge states of 3D QHE in topological semimetals are located at two diagonal hinges (boundaries of surface). Their positions switch to the

* Corresponding authors.
E-mail addresses: yanmou@zzu.edu.cn (M. Yan), zyliu@whu.edu.cn (Z. Liu), chengang971@163.com (G. Chen).
[1] These authors contributed equally to this work.

https://doi.org/10.1016/j.scib.2024.04.055
2095-9273/

other two diagonal hinges when the magnetic field is reversed [23,27–30]. However, these edge states have not yet been directly observed experimentally.

In this work, we experimentally observe the edge states of 3D QHE based on acoustic crystals (ACs), which are the artificial periodical structure with frequency bands in reciprocal space for acoustic waves. Benefiting from the macroscopic nature, the ACs have been demonstrated to be ideal platforms for observing various exotic states in topological physics [31–35]. As the magnetic field has no effect on acoustic waves, a counterpart, referred to as the pseudo-magnetic field (PMF), has to be constructed with an effect on acoustic waves similar to that of the magnetic field on electrons. A common strategy for constructing the PMF for acoustic waves is to introduce the structural gradient [36,37], and as such the acoustic QHE in 2D systems [38–42] and acoustic chiral Landau levels in 3D Weyl systems [41,42] have all been observed. Here, we design an acoustic Weyl semimetal by stacking the hexagonal lattice. By introducing a structural gradient along an armchair direction in the hexagonal plane, a uniform PMF with direction parallel to the plane is created. Specially, the PMF is perpendicular to the Fermi arcs on the opposite side surfaces so that the Landau plateaus can be created for both the bulk and the arc surface states. The surface Landau levels give rise to the unique edge states, which is the signal of 3D QHE in the acoustic Weyl semimetal. The theoretical, simulated, and experimental results are in good agreement.

2. Theoretical model

Fig. 1a shows a schematic of an A-A stacking hexagonal lattice along the z direction. The hexagonal lattice contains two sites A (red sphere) and B (blue sphere) with the opposite on-site energies $\pm\varepsilon$, and possesses the nearest-neighbor hopping t_1 (gray tube) and next-nearest-neighbor hopping t_2 (yellow tube). For two adjacent layers, they are connected by the interlayer hoppings t_a (red tube) and t_b (blue tube). The lattice constants in the x-y plane and along the z direction are a and h, respectively. This stacking structure with $t_a t_b < 0$ is identified as an ideal type-I Weyl semimetal, hosting four Weyl points at $\bar{K}_{\pm}(4\pi/3a, 0, \pm k_W/h)$ and their time-reversal counterparts $\bar{K}'_{\pm}(-4\pi/3a, 0, \pm k_W/h)$, with $k_W = \arccos[\varepsilon/(t_b - t_a)]$ (see Supplementary materials Section 1). The eigenvalues of Weyl points are $\epsilon_0 = (t_a + t_b)\varepsilon/(t_b - t_a) - 3t_2$. These Weyl points induce nontrivial surface bands in the k_x-k_z plane, whose equi-energy contours form the open Fermi arcs connecting the projection of $\bar{K}_+$ and $\bar{K}'_+$ ($\bar{K}_-$ and $\bar{K}'_-$) on the front and back surfaces (see Supplementary materials Section 2).

When energy is at the Weyl points ($E = \epsilon_0$), the open Fermi arcs on different surfaces can be connected with the assistance of Weyl points with the opposite charges, forming the closed Fermi loop [23,27]. In the electronic materials, when the Fermi loop is disturbed by external magnetic fields, the 3D QHE is generated [22,23,27–30]. However, sound cannot respond to the external

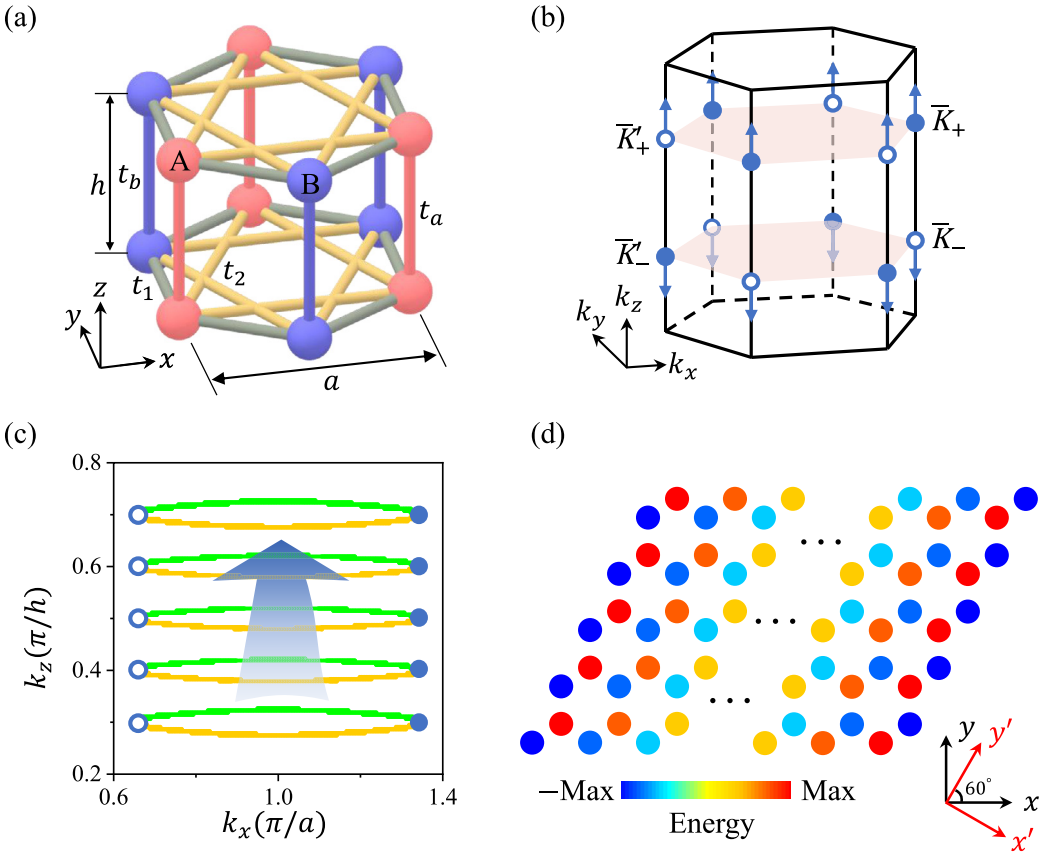

Fig. 1. (Color online) Pseudo-magnetic field induced by the inhomogeneous structure. (a) Schematics of the A-A stacking hexagonal lattice. (b) First Brillouin zone and the distribution of the Weyl points. The Weyl points hosting opposite topological charges are denoted by the hollow and solid circles, and the arrows show their shifts along the $\pm k_z$ directions by changing the on-site energies of A and B. (c) The equi-energy contours of the surface states at the energy of Weyl points ($E = 0.3$) with different on-site energies. The yellow and green curves represent respectively the Fermi arcs in front and back surfaces when the Weyl points are located at $k_z h/\pi = 0.3$, 0.4, 0.5, 0.6 and 0.7. The arrow indicates the shifting direction of the Fermi arcs. (d) Inhomogeneous configuration with gradient on-site energy along the x' direction. The plotted parameters in (c) are chosen as $t_1 = -1$, $t_2 = -0.1$, $t_a = 0.8$, $t_b = -0.8$ and $\gamma = 0.01$ in arbitrary unit (a.u.).

magnetic fields, so we have to construct PMF by engineering the structures [37–45].

Note that when the on-site energy ε increased, the pair of Weyl points $\bar{K}_+$ and $\bar{K'}_+$ ($\bar{K}_-$ and $\bar{K'}_-$) move along the positive (negative) k_z directions as shown in Fig. 1b. Meanwhile, the Fermi arcs connecting the projection of $\bar{K}_+$ and $\bar{K'}_+$ ($\bar{K}_-$ and $\bar{K'}_-$) on the front and back surfaces also have the same movement trajectory as these Weyl points, monotonically shifting along the k_z direction, as shown in Fig. 1c. This means that we can realize the PMF by introducing gradient on-site energy [46]. As shown in Fig. 1d, the gradient of the on-site energy is along the x' direction (30° with respect to the x direction) and assumed as $\varepsilon_{x'} = \varepsilon(1 + \gamma x')$, with γ being the structural parameter. Specifically, near the Weyl points $\bar{K}_+$ and $\bar{K'}_+$, the PMF $\boldsymbol{B} = \varepsilon\gamma/[(t_a - t_b)h\sin(k_W)]\boldsymbol{e}_{y'}$, where $\boldsymbol{e}_{y'}$ is a unit vector along the y' direction (see Supplementary materials Section 3), induces the valley dependent chiral Landau level with the opposite group velocity direction, as shown in Fig. 2a and b. For the Weyl points $\bar{K}_-$ and $\bar{K'}_-$, both the charges and the direction of pseudo-magnetic field are reversed, leading to the same chiral Landau levels as $\bar{K}_+$ and $\bar{K'}_+$.

Since the PMF has the component which is perpendicular to the Fermi arcs on the opposite side surfaces, the mentioned Fermi loop that is composed of Fermi arcs and Weyl points splits hence into the discrete Landau plateaus. To elucidate this, we choose a finite parallelogram-shaped structure in the x-y plane and present the projected dispersion along the k_z direction, as shown in Fig. 2c. It indicates that these discrete Landau plateaus exist in the gap of ±1 st Landau levels (gray regions in Fig. 2a and b) of the bulk. In contrast to the traditional 2D QHE whose Landau plateaus are localized in the bulk, here the Landau plateaus are created for both the bulk and the arc surface states (see Supplementary materials Section 5). At the boundary of the surfaces, the Landau plateaus deform and then induce the edge states localized on the diagonal hinges, which is the signature of 3D QHE [20,21]. In Fig. 2d, we plot spatial distributions of the edge states marked by the red and blue dots in Fig. 2c. This figure shows that on the front (back) surface, the edge states distribute in the left (right) side. Noted that the projected dispersion is dependent on the shape of the plate structure. For example, by choosing a rectangular plate structure, the projected dispersion changed (as discussed in Supplementary materials Section 5) and different from the case of parallelogram-shaped structure, but the hinge states are still exist.

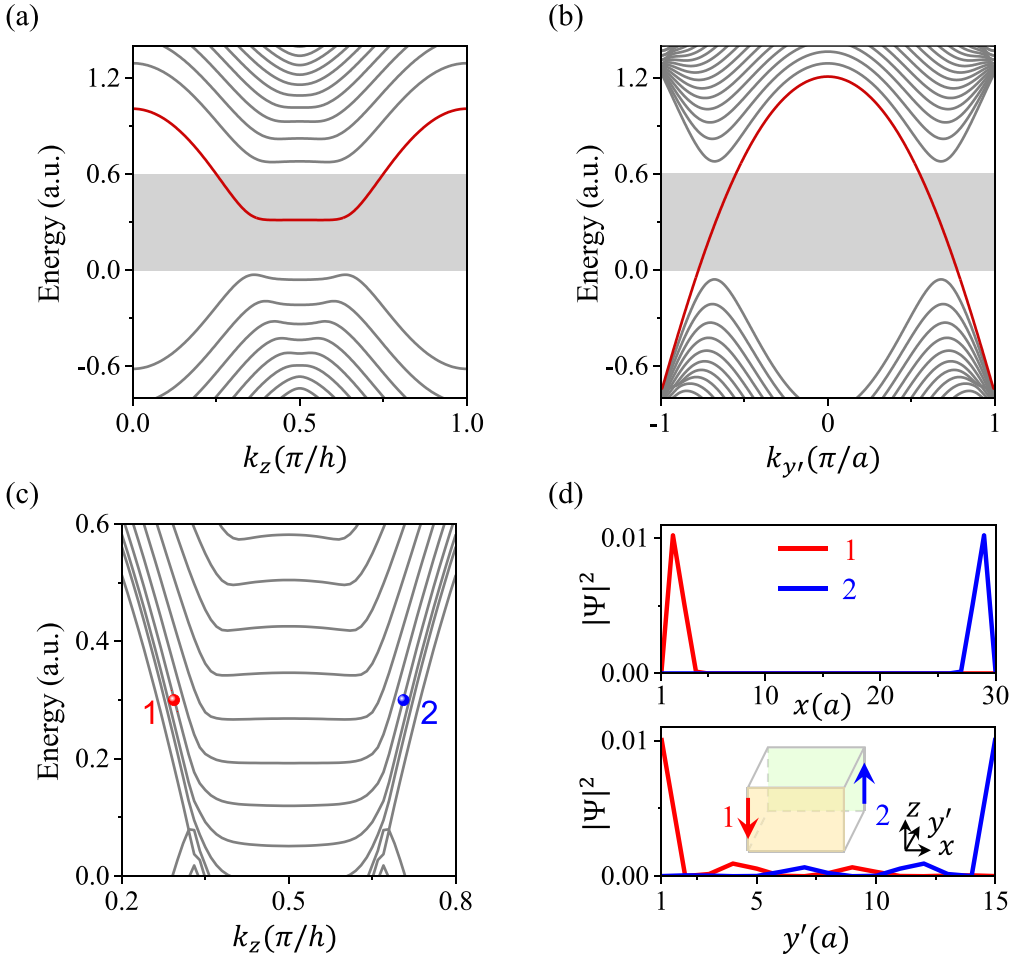

Fig. 2. (Color online) Edge states of 3D quantum Hall effect induced by pseudo-magnetic field. (a), (b) Projected dispersions along the k_z direction for $k_{y'} = 4\pi/3a$ (a) and along the $k_{y'}$ direction for $k_z = 0.5\pi/h$ (b). The red and gray curves denote the chiral Landau levels and other Landau levels. (c) Projected dispersions of a parallelogram-shaped structure along the k_z direction. (d) Wave function distributions of the edge states (red and blue dots in (c)) along the x (top panel) and y' (bottom panel) directions. Inset: schematics of the parallelogram-shaped plate structure with thickness $30a$ (x) and width $15a$ (y'). The red and blue arrows represent the edge states. The plotted parameters are same as Fig. 1c.

3. Results and discussion

To demonstrate experimentally the exotic edge states of 3D QHE, we construct the acoustic Weyl system in an AC based on the stacked hexagonal lattice with the lattice constants $a = 34.64$ mm and $h = 34.00$ mm. The side and top views of the unit cell are shown in Fig. 3a. The hexagonal lattice consists of two cylindrical cavities (marked A and B) connected by the intra- and inter-layer square tubes. For cavity A, the cylinders (red region) with diameter $s = 9.00$ mm and height $d_1 = 0.60$ mm are added on the top and bottom surfaces, while for cavity B, the other cylinders (blue region) with different height $d_2 = 0.50$ mm are subtracted from cavity B. More detailed parameters are shown in Supplementary materials Section 6. Based on the simulation by the COMSOL Multiphysics, this acoustic system hosts four Weyl points $(\pm 4\pi/3a, 0, \pm 0.18\pi/h)$ at the frequency of 7.98 kHz, which is in good agreement with the tight-binding calculation (see Supplementary materials Section 7). To control the shifts of Weyl points along the k_z direction, we elaborately design nine distinct unit cells with different d_1 and d_2, as shown in Table 1. Arranging these unit cells along the x' direction, a 3D-printed inhomogeneous AC is shown in Fig. 3b. This sample is a prism with a height 680.00 mm and the cross section is a rhombus with a side length 311.76 mm.

To confirm the existence of the PMF, we first observe the chiral Landau level in the inhomogeneous AC. Since the time-reversal and mirror symmetries of the AC are conserved, here we only focus on the physics near Weyl point $\bar{K}_+$ for simplicity. A point source is successively placed at the centers of the 3-rd, 5-th, and 7-th column on the front surface, marked by the red stars P_1, P_2 and P_3 in Fig. 3b. A detector scans respectively the overall acoustic pressure field of the y'-z plane where the point source is located. The detected signal intensity in the momentum space relies strongly on the source position, where the local eigen states are strongly excited. With a discrete Fourier transform along the y' and z directions, we obtain the distributions of field amplitude in the momen-

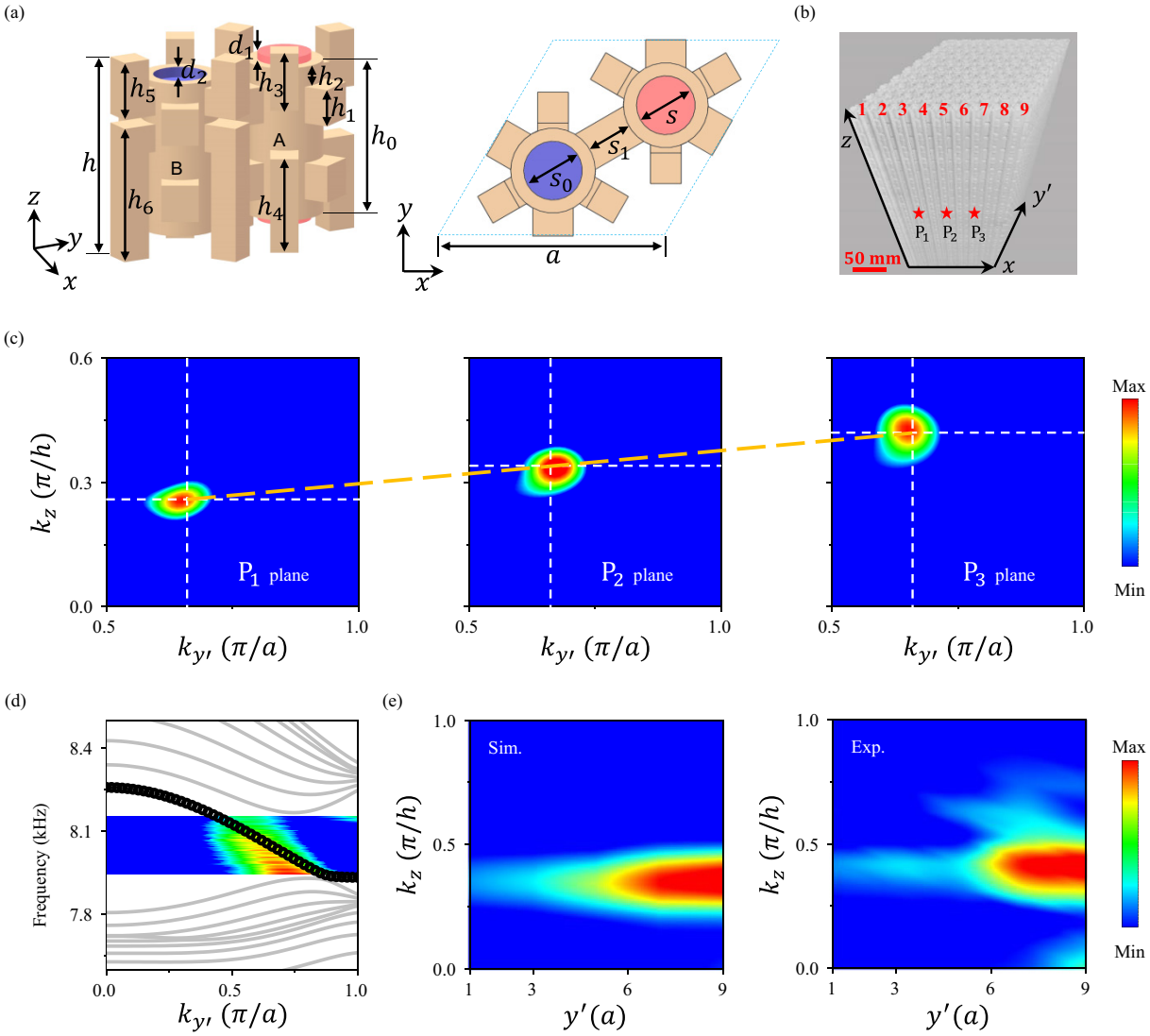

Fig. 3. (Color online) Acoustic chiral Landau levels. (a) Side (left panel) and top (right panel) views of a unit cell. (b) A photo of the 3D-printed inhomogeneous acoustic crystal and the red numerals indicate the columns of the sample. The point sources are denoted by the red stars. (c) Measured equi-frequency contours interpreted as Weyl points with a linear space-dependent shift in the $k_{y'}$-k_z plane at the excitation frequency of 7.98 kHz, when the point source is successively placed at P_1 (left panel), P_2 (middle) and P_3 (right panel). The intersections of the white dashed-lines in left panel, middle, and right panel represent different positions of the zeroth Landau plateau corresponding to $k_z h/\pi = 0.26$, 0.34, and 0.42, respectively. (d) Projected dispersion along the $k_{y'}$ direction for $k_z = 0.34\pi/h$. The black hollow circles and gray lines represent the simulated chiral Landau level and other Landau levels, respectively. The color maps represent the experiment data in the frequency range of 7.95 to 8.15 kHz. (e) Simulated (left panel) and measured (right panel) acoustic pressure field distributions along the y' direction for different k_z at the frequency of 7.98 kHz.

Table 1
Values of the geometrical parameters and locations of Weyl points (WPs) for each unit cell (UC) of the acoustic crystal.

	d_1(mm)	d_2(mm)	WPs
UC1	0.60	0.50	$(\pm 4\pi/3a, 0, \pm 0.18\pi/h)$
UC2	1.15	0.95	$(\pm 4\pi/3a, 0, \pm 0.22\pi/h)$
UC3	1.75	1.25	$(\pm 4\pi/3a, 0, \pm 0.26\pi/h)$
UC4	2.25	1.45	$(\pm 4\pi/3a, 0, \pm 0.30\pi/h)$
UC5	2.92	1.62	$(\pm 4\pi/3a, 0, \pm 0.34\pi/h)$
UC6	3.50	1.80	$(\pm 4\pi/3a, 0, \pm 0.38\pi/h)$
UC7	4.20	1.90	$(\pm 4\pi/3a, 0, \pm 0.42\pi/h)$
UC8	5.10	1.90	$(\pm 4\pi/3a, 0, \pm 0.46\pi/h)$
UC9	6.85	1.65	$(\pm 4\pi/3a, 0, \pm 0.50\pi/h)$

tum space of $k_{y'}$-k_z plane at the frequency of 7.98 kHz, as shown in Fig. 3c. The Weyl point corresponding to the positions $k_z h/\pi = 0.26$ (left panel), 0.34 (middle), and 0.42 (right panel), reveal the linearly space-dependent shifts in the AC as marked by the orange dashed line. Thus, a uniform acoustic PMF with the magnitude $B_b = 0.02\pi/ha$ is generated. Because the time reversal symmetry is not broken in the system, the pseudo-magnetic field adds up to zero throughout the whole AC, and the net flux in the system is zeros.

In Fig. 3d, we simulate the projected dispersions along the $k_{y'}$ direction for $k_z = 0.34\pi/h$, which clearly shows the existence of the chiral Landau level (black hollow circles). To observe the chiral Landau level, we put the source at the center of the back surface to excite the acoustic pressure field due to the negative group velocity along the y' direction. By scanning the frequency in the range of 7.95 to 8.15 kHz (the gap of ±1 st Landau levels), we obtain the dispersion of the chiral Landau level, as shown by the inserted color map in Fig. 3d. In addition, we take the acoustic pressure field of y'-z plane in the center of the AC at the frequency of 7.98 kHz, and perform Fourier transform along the z direction, acquiring the field distributions for different k_z (Fig. 3e). The measured and simulated results are in good agreement and indicate that the acoustic pressure field is mainly localized at $k_z = 0.34\pi/h$ and propagates along the negative y' direction.

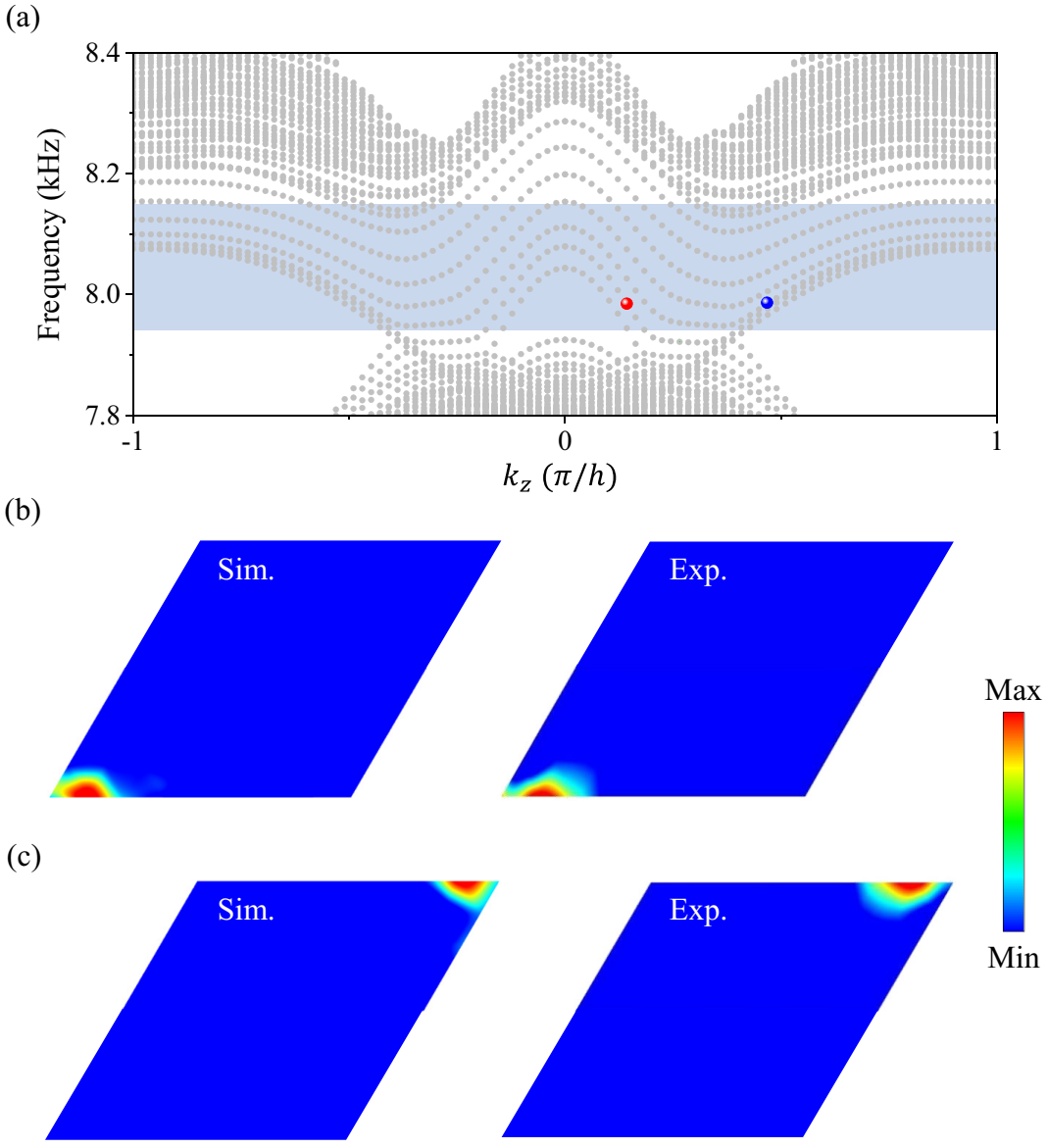

Fig. 4. (Color online) 3D acoustic quantum Hall effect. (a) Simulated projected dispersion of a rhombus acoustic crystal structure along the k_z direction. The shadow region represents the frequency from 7.95 to 8.15 kHz. (b), (c) Measured (left panel) and simulated (right panel) acoustic pressure field distributions of the edge states at the excitation frequency around 7.98 kHz for $k_z h/\pi = 0.20$ (b) and 0.44 (c), corresponding to the red and blue dots in (a), respectively.

Fig. 4a shows the simulated projected dispersion along the k_z direction, where the supercell is chosen as the parallelogram-shaped plate structure. In the frequency range of 7.95 to 8.15 kHz (shadow region), a series of Landau plateaus are formed. According to the eigen-simulation (see Supplementary materials Section 9), the acoustic pressure fields on these Landau plateaus are localized on the bulk and side surfaces. Close to the boundary of the surface, the plateaus deform and give rise to the edge states of the 3D QHE. The acoustic pressure fields of the edge states, such as the red and blue dots in Fig. 4a, are localized on the left edge of the front surface and right edge of the back surface.

Since the edge state marked by the red dot in Fig. 4a has the negative group velocity, we put the point source at the top surface of the sample and measure the whole acoustic pressure field in the AC. After the Fourier transformation, we obtain the acoustic pressure field distribution for $k_z = 0.20\pi/h$ at the frequency around 7.98 kHz, as shown in Fig. 4b. The measured field distribution clearly demonstrates the existence of the edge state located on the left side of the front surface. To observe the edge state marked by the blue dot in Fig. 4a, we place the point source at the top surface of the sample (Supplementary materials Section 9). Fig. 4c shows the measured acoustic pressure field distribution for $k_z = 0.44\pi/h$ at the same frequency. This figure shows that the edge state is located in the right side of the back surface, as expected. The experimental observations (right panels) shown by the right panel of Fig. 4b and c agree well with the simulated results (left panels).

4. Conclusion

In summary, we have theoretically proposed and experimentally demonstrated the 3D acoustic quantum Hall states in Weyl AC. A uniform acoustic PMF is created with the introduction of a structural gradient, and as a result, the Fermi loop formed by the bulk and arc surface states splits into the discrete Landau plateaus. The unique chiral edge transport, with sound pinned on the boundaries of opposite surfaces, is visualized. This novel sound manipulation can not only serve as the basis for acoustic devices with unconventional functions, but also lay the foundation for continuing exploring the 3D Hall physics. An interesting question is whether there are higher-order corner states in 3D quantum Hall system. This has not been previously investigated, and as an initial exploration, we give an example in Supplementary materials Section 10.

Conflict of interest

The authors declare that they have no conflict of interest.

Acknowledgments

This work was supported by the National Key R & D Program of China (2022YFA1404500, 2022YFA1404900), the National Natural Science Foundation of China (11890701, 11974120, 11974005, 12034012, 12074128, 12074232, 12125406, 12204290, and 12374360), the National Postdoctoral Program (BX20220195 and 2023M732146), Shanxi "1331 Project", and Cross-disciplinary Innovative Research Group Project of Henan Province (232300421004). We were grateful to Zhi-Qiang Zhang, Hai-Long Li, and Hai-Peng Sun for fruitful discussions.

Author contributions

Gang Chen, Zhengyou Liu, Mou Yan, and Suotang Jia conceived the idea. Qiang Wei and Xuewei Zhang calculated the theoretical results, carried out the numerical simulations and designed the experiments. Qiang Wei, Xuewei Zhang, and Mian Peng performed the experiments. Weiyin Deng, Jiuyang Lu, and Xueqin Huang guided the experimental measurement and analyzed the experimental data. Qiang Wei, Mou Yan, Zhengyou Liu, and Gang Chen supervised the project. All the authors contributed to the preparation of the manuscript.

Appendix A. Supplementary materials

Supplementary materials to this article can be found online at https://doi.org/10.1016/j.scib.2024.04.055.

References

[1] Klitzing K, Dorda G, Pepper M. New method for high-accuracy determination of the fine-structure constant based on quantized Hall resistance. Phys Rev Lett 1980;45:494–7.
[2] Tsui D, Stormer H, Gossard A. Two-dimensional magnetotransport in the extreme quantum limit. Phys Rev Lett 1982;48:1559–62.
[3] Haldane F. Model for a quantum Hall effect without Landau levels: Condensed-matter realization of the "parity anomaly". Phys Rev Lett 1988;61:2015–8.
[4] Kane CL, Mele EJ. Quantum spin Hall effect in graphene. Phys Rev Lett 2005;95:226801.
[5] Hasan MZ, Kane CL. Colloquium: Topological insulators. Rev Mod Phys 2010;82:3045–67.
[6] Qi XL, Zhang SC. Topological insulators and superconductors. Rev Mod Phys 2011;83:1057–110.
[7] Xie L, Jin L, Song Z. Antihelical edge states in two-dimensional photonic topological metals. Sci Bull 2023;68:255–8.
[8] Wu SQ, Cheng W, Liu XY, et al. Observation of D-class topology in an acoustic metamaterial. Sci Bull 2024;69:893–900.
[9] Chen L, Chen P, Li W, et al. Enhancement of thermoelectric performance across the topological phase transition in dense lead selenide. Nat Mater 2019;18:1321.
[10] Han F, Andrejevic N, Nguyen T, et al. Quantized thermoelectric Hall effect induces giant power factor in a topological semimetal. Nat Commun 2020;11:6167.
[11] Wang AQ, Xiang PZ, Zhao PZ, et al. Topological nature of higher-order hinge states revealed by spin transport. Sci Bull 2022;67:788–93.
[12] Störmer H, Eisenstein J, Gossard A, et al. Quantization of the Hall effect in an anisotropic three-dimensional electronic system. Phys Rev Lett 1986;56:85–8.
[13] Halperin B. Possible states for a three-dimensional electron gas in a strong magnetic field. Jpn J Appl Phys 1987;26:1913–9.
[14] Kohmoto M, Halperin B, Wu Y. Diophantine equation for the three-dimensional quantum Hall effect. Phys Rev B 1992;45:13488–93.
[15] Koshino M, Aoki H, Kuroki K, et al. Hofstadter butterfly and integer quantum Hall effect in three dimensions. Phys Rev Lett 2001;86:1062–5.
[16] Bernevig B, Hughes T, Raghu S, et al. Theory of the three-dimensional quantum Hall effect in graphite. Phys Rev Lett 2007;99:146804.
[17] Wang P, Ren Y, Tang F, et al. Approaching three-dimensional quantum Hall effect in bulk $HfTe_5$. Phys Rev B 2020;101. 161201(R).
[18] Zhang C, Narayan A, Lu S, et al. Evolution of Weyl orbit and quantum Hall effect in Dirac semimetal Cd_3As_2. Nat Commun 2017;8:1272.
[19] Uchida M, Nakazawa Y, Nishihaya S, et al. Quantum Hall states observed in thin films of Dirac semimetal Cd_3As_2. Nat Commun 2017;8:2274.
[20] Schumann T, Galletti L, Kealhofer D, et al. Observation of the quantum Hall effect in confined films of the three-dimensional Dirac semimetal Cd_3As_2. Phys Rev Lett 2018;120:016801.
[21] Tang F, Ren Y, Wang P, et al. Three-dimensional quantum Hall effect and metal-insulator transition in $ZrTe_5$. Nature 2019;569:537–41.
[22] Zhang C, Zhang Y, Yuan X, et al. Quantum Hall effect based on Weyl orbits in Cd_3As_2. Nature 2019;565:331–6.
[23] Wang C, Sun H, Lu H, et al. 3D quantum Hall effect of Fermi arcs in topological semimetals. Phys Rev Lett 2017;119:136806.
[24] Wan X, Turner A, Vishwanath A, et al. Topological semimetal and fermi-arc surface states in the electronic structure of pyrochlore iridates. Phys Rev B 2011;83:205101.
[25] Armitage N, Mele E, Vishwanath A. Weyl and Dirac semimetals in three-dimensional solids. Rev Mod Phys 2018;90:015001.
[26] Lu YH, Wang BZ, Liu XJ. Ideal Weyl semimetal with 3D spin-orbit coupled ultracold quantum gas. Sci Bull 2020;65:2080–5.
[27] Chen R, Liu T, Wang C, Lu H, et al. Field-tunable one-sided higher-order topological hinge states in Dirac semimetals. Phys Rev Lett 2021;127:066801.
[28] Li H, Liu H, Jiang H, et al. 3D quantum Hall effect and a global picture of edge states in Weyl semimetals. Phys Rev Lett 2020;125:036602.
[29] Chen R, Wang CM, Liu T, et al. Quantum Hall effect originated from helical edge states in Cd_3As_2. Phys Rev Research 2021;3:033227.
[30] Zhang X, Nagaosa N. Anisotropic three-dimensional quantum Hall effect and magnetotransport in mesoscopic Weyl semimetals. Nano Lett 2022;22:3033–9.

[31] Weiner M, Ni X, Li M, et al. Demonstration of a third-order hierarchy of topological states in a three-dimensional acoustic metamaterial. Sci Adv 2020;6:aay4166.
[32] Ni X, Li M, Weiner M, et al. Demonstration of a quantized acoustic octupole topological insulator. Nat Commun 2020;11:2108.
[33] Xue H, Ge Y, Sun H, et al. Observation of an acoustic octupole topological insulator. Nat Commun 2020;11:2442.
[34] Li JK, Mo Q, Jiang JH, et al. Higher-order topological phase in an acoustic fractal lattice. Sci Bull 2022;67:2040–4.
[35] Huang XQ, Lu JY, Yan Z, et al. Acoustic higher-order topology derived from first-order with built-in Zeeman-like fields. Sci Bull 2022;67:488–94.
[36] Brendel C, Peano V, Painter OJ, et al. Pseudomagnetic fields for sound at the nanoscale. Proc Natl Acad Sci USA 2017;114:E3390–5.
[37] Abbaszadeh H, Souslov A, Paulose J, et al. Sonic Landau levels and synthetic gauge fields in mechanical metamaterials. Phys Rev Lett 2017;119:195502.
[38] Yang Z, Gao F, Yang Y, et al. Strain-induced gauge field and Landau levels in acoustic structures. Phys Rev Lett 2017;118:194301.
[39] Wen X, Qiu C, Qi Y, et al. Acoustic Landau quantization and quantum-Hall-like edge states. Nat Phys 2019;15:352–6.
[40] Yan M, Deng W, Huang X, et al. Pseudomagnetic fields enabled manipulation of on-chip elastic waves. Phys Rev Lett 2021;127:136401.
[41] Peri V, Serra-Garcia M, Ilan R, et al. Axial-field-induced chiral channels in an acoustic Weyl system. Nat Phys 2019;15:357–61.
[42] Ilan R, Grushin AG, Pikulin DI. Pseudo-electromagnetic fields in 3D topological semimetals. Nat Rev Phys 2020;2:29–41.
[43] Jia H, Zhang R, Gao W, et al. Observation of chiral zero mode in inhomogeneous three-dimensional Weyl metamaterials. Science 2019;363:148–51.
[44] Grushin AG, Venderbos JWF, Vishwanath A, et al. Inhomogeneous Weyl and Dirac semimetals: Transport in axial magnetic fields and fermi arc surface states from pseudo-Landau levels. Phys Rev X 2016;6:041046.
[45] Pikulin DI, Chen A, Franz M. Chiral anomaly from strain-induced gauge fields in Dirac and Weyl semimetals. Phys Rev X 2016;6:041021.
[46] Kiriushechkina S, Vakulenko A, Smirnova D, et al. Spin-dependent properties of optical modes guided by adiabatic trapping potentials in photonic Dirac metasurfaces. Nat Nanotechnol 2023;18:875–81.

Xuewei Zhang received his bachelor's degree in physics from Shanxi University in 2019, and subsequently pursued his Ph.D. degree at the Institute of Laser Spectroscopy, Shanxi University. Currently, he is a visiting student at the School of Physics, Zhengzhou University. His research interest includes the simulation of novel topological states of matter in phononic crystals and circuit systems, as well as the simulation of non-Hermitian systems.

Qiang Wei is currently a postdoctoral fellow at Shanxi University. He received his Ph.D. degree in Physics from Shanxi University in 2022. His research interest is mainly in the topological states and the corresponding physical properties using phonon crystals.

Mou Yan is an assistant research fellow at the School of Physics and Laboratory of Zhongyuan Light, Zhengzhou University. He received his Ph.D. degree from South China University of Technology in 2019. His research interest is the topological phononic crystals and metamaterials, including sonic and elastic topological materials.

Zhengyou Liu received his Ph.D. degree in 1993 from Wuhan University. Before he joined Wuhan University in 2001, he held the position of professor at South China University of Technology. He is currently a professor at the School of Physics and Technology. His current research interest includes wave physics, phononic crystals and acoustic metamaterials, acoustic radiation force and particle manipulation, and topological acoustics.

Gang Chen received his Ph.D. degree in 2009 from Shanxi University and had a postdoctoral research in Washington State University from 2010 to 2011. He was a professor at the State Key Laboratory of Quantum Optics and Quantum Optics Devices in Shanxi University. In 2022, he joined Zhengzhou University as full professor of physics. His current research interest includes ultracold atom, quantum optics, and acoustics crystals.